COMPLEX DOMAIN SPARSE PHASE IMAGING BASED ON NONLOCAL BM3D TECHNIQUES*

VLADIMIR KATKOVNIK † AND KAREN EGIAZARIAN ‡

Abstract. The paper is addressed to 2D phase and amplitude estimation of complex-valued signals – that is, in particular, to estimation of modulo-2π interferometric phase images from periodic and noisy observations. These degradation mechanisms make phase image estimation a challenging problem. A sparse nonlocal data-adaptive imaging formalized in complex domain is used for phase and amplitude image reconstruction. Following the procedure of patch-based technique, the image is partitioned into small overlapping square patches. Block Matching Three Dimensional (BM3D) technique is developed for forming complex domain sparse spectral representations of complex-valued data. HOSVD applied to BM3D groups enables the design of the orthonormal complex domain 3D transforms which are data adaptive and different for each BM3Ds group. An iterative version of the complex domain BM3D is designed from variational formulation of the problem. The convergence of this algorithm is shown. The effectiveness of the new sparse coding based algorithms is illustrated in simulation experiments where they demonstrate the state-of-the-art performance.

Key words. complex domain image denoising, complex domain sparsity, phase imaging, nonlocal block matching, HOSVD.

AMS subject classification. 62H35, 62H12, 68U10, 94A08.

1. Introduction. This paper is focussed on a special wide class imaging problems concerning wavefield/wavefront sensing and reconstruction. In particular, a monochromatic coherent wavefield is modelled by complex amplitude $u = ae^{j\varphi}$, where a is an amplitude and φ is a phase of the wavefield. In modern technology and science phase and wavefield imaging are popular and well established technique for high-accuracy measuring, recording and reconstructing 2D and 3D objects. The areas of applications are varying from astronomy and engineering to medicine and biology [1], [2]. In engineering phase and wavefield sensing methods serve for nondestructive testing/control and precise measurements (e.g. [3] - [6]). In medicine and biology phase measurements are exploited in microscopy and coherent tomography, for instance in Fourier phase microscopy. We wish to mention also such developments as the phase based registration of brain dynamics, express blood tests, measurement of biological structures in body tissues.

The topic of sparse and redundant representations has attracted tremendous interest in the last ten years. This interest is defined by the fundamental role that the low dimensional models play in many signal and image processing areas such as compression, restoration, classifications, and design of priors and regularizers, just to name a few. It is assumed in sparse imaging that there exists a basis consisting of a small number of items where image can be represented exactly or approximately with a good accuracy. This ideal basis is a priory unknown and selected from a given set of potential bases (dictionary or dictionaries) or designed from given noisy observations. Sparse representation can be treated as a regression approximation of signals with an adaptive basis selection, one of the classical topics in statistics. The modern popularity and success of sparse representation are mainly due to the efficient algorithms and

*This work is supported by the Academy of Finland, project no. 138207.

†Department of Signal Processing, Technology University of Tampere, Tampere, Finland, 33720 (vladimir.katkovnik@tut.fi).

‡Department of Signal Processing, Technology University of Tampere, Tampere, Finland, 33720 (karen.egiazarian@tut.fi).

the multiple evidence that this type of mathematical modeling meats requirements of many important applications. The compressive (or compressed) sensing (CS) is one of the fields where sparse representation techniques are efficient. In CS, the object distribution image is reconstructed from subsampled data. A total number of available observations can be smaller (much smaller) than the size of the image. It is proved in CS that the perfect reconstruction from the subsampled data can be achieved for sparse images. To add yet more interest to this imaging techniques, the dictionaries yielding sparse representations may be learned from the data they represent. Dictionary learning is currently one of the hottest research topics in the area of sparse imaging [7].

Recently in optics, sparse imaging in complex domain has become a subject of multiple applications. Complex-valued data and operators are distinctive features of this development. Basic facts of the corresponding theory, algorithms, simulations as well as experimental demonstrations can be found in [8], [9]. In the works concerning the complex-valued data the phase is the most delicate and difficult issue and the corresponding dictionary design for sparse modeling is crucial. It is demonstrated in [10] a strong improvement in CS hyperspectral imaging due to the quadratic penalization for phase used jointly with the TV penalty for the complex-valued wavefield. A serious accuracy improvement for the wavefield reconstruction was demonstrated in [11] - [13] due to a sparse modeling separate for amplitude and absolute phase. A regularization of amplitude and interferometric phase through the total variation penalties is introduced in [14] for wavefield reconstruction in digital holography.

In this paper, we design complex domain synthesis and analysis transforms (dictionaries) imposing the sparsity in the transform complex domain, i.e. dealing with phase and amplitude simultaneously. Our design is based on Block Matching Three Dimensional (BM3D) paradigm. The complex-valued image is partitioned into small overlapping rectangular patches. For each patch, a group of similar patches is collected from a pre-defined neighborhood and stacked together forming a 3D array. The BM3D analysis transform is then applied to the group. The obtained spectral coefficients are manipulated (hard/soft-thresholded) and the collaboratively filtered patches synthesized with the BM3D synthesis transform. This process is repeated over the entire image and the obtained overlapped filtered patches are aggregated in the final image estimate.

BM3D as it is presented in [15] for the complex domain is modified in two ways. First, patching and grouping of similar patches are applied to complex-valued variables. Second, we adopt third order HOSVD (see, e.g., [16] - [18]) as an analysis transform. After applying HOSVD to the 3D groups, we obtain complex-valued group-wise spectrums and three orthonormal complex domain transforms: two for each coordinate of 2D patches and the third one for the longitudinal coordinate of the group. Thus, instead of the fixed real-valued analysis transforms originally proposed in BM3D [15], we obtain group-dependent and complex-valued transforms, where phases and amplitude are linked. This new technique can be understood as a generalization for the complex domain of the BM3D-SAPCA algorithm [19], where SVD is used for design of 2D orthonormal bases for patches, and also of HOSVD-BM3D proposed in [20], where HOSVD is exploited as a generator of 3D/4D real domain orthonormal transforms.

A different approach to complex domain filtering is developed in the recent paper [21] based on the dictionary leaning incorporated in patch-based image restoration. Aiming at optimal sparse representations, and thus at optimal noise removing capabil-

ities, the dictionary is learned from the data that it represents via matrix factorization with sparsity constraints on the code (i.e., the regression coefficients) enforced by the l_1-norm. Two types of the dictionaries are studied: externally designed from sets of clear images (extra data) and internally designed from noisy data obtained for the image of interest only.

The complex domain BM3D incorporating HOSVD was proposed in [22] as a heuristic straightforward generalization of the real-valued BM3D [15]. In this paper we are focussed on transform domain sparse representations for complex-valued variables and using it for denoising algorithm design. The contribution of this paper concerns the following aspects of the problem: (1) Complex domain sparsity modeling and the complex domain BM3D algorithm; (2) Sparsity optimization and designing an iterative complex domain BM3D; (3) The complex domain BM3D as a nonexpansive operator and convergence proof for the iterative algorithm; (4) Extended simulation experiments confirming the state-of-the-art performance of the developed algorithms.

In what follows the paper is organized as follows. The observation model and the complex domain BM3D algorithm are presented in Section 2. Links of this algorithm with sparsity modeling is a subject of Section 3. The iterative complex domain BM3D is derived in this section and the convergence proof is given for this algorithm. An extensive experimental study of the complex domain BM3D and its iterative version is a subject of Section 4. These experiments show that the iterative algorithm enables a better performance and the both algorithms are the state-of-the-art in the field.

2. Complex domain BM3D . Let us assume that the observed data $z : X \to C$, where $X \subset Z^2$ is $2D$ grid of size $\sqrt{n} \times \sqrt{n}$, are modeled as

$$\begin{aligned} z(x) &= u(x) + \varepsilon(x), \\ u(x) &= a(x)e^{j\varphi(x)}, \end{aligned} \tag{2.1}$$

where $x \in X$, $u(x) \subset \mathbb{C}^{\sqrt{n}\times\sqrt{n}}$ is a clear complex-valued image, and $\varepsilon(x) = \varepsilon_I(x) + j\varepsilon_Q(x) \subset \mathbb{C}^{\sqrt{n}\times\sqrt{n}}$, is complex-valued zero-mean Gaussian circular white noise of variance σ^2 (i.e., ε_I and ε_Q are zero-mean independent Gaussian random variables with variance $\sigma^2/2$).

2.1. CD-BM3D algorithm . We start from presentation of the complex domain BM3D (CD-BM3D) as it is proposed in [22]. The abbreviation CD-BM3D is introduced in this paper in order to emphasize succession of this algorithm with respect to BM3D.

Following the procedure in patch-based image restoration, the noisy $\sqrt{n} \times \sqrt{n}$ image $\mathbf{z} \equiv \{z(x),\, x \in X\}$ is partitioned into small overlapping rectangular/square patches $N_1 \times N_2$ defined for each pixel of the image. The basic steps of the algorithm are as follows: grouping, HOSVD transform of 3D groups, hard-thresholding of HOSVD spectrum, inverse HOSVD transform, and aggregation of the overlapping patch estimates. Compared with [15], we have two major differences: a) the images are complex-valued; b) the transform used to carry out a 3D filtering is the HOSVD, which brings groupwise transform adaptiveness not present in [15]. Similar to [22] these steps can be detailed as follows.

1. **Grouping**

Let $\mathbf{P}_x \equiv \{z(y),\, y \in \mathcal{P}_x \subset X\}$ denotes an image patch of size $N_1 \times N_2$ defined on the domain $\mathcal{P}_x$, where the index $x \in X$ corresponds to the upper-left pixel of the patch. For each $r-th$ patch (reference patch) we select J_r similar patches which are

closest to the reference patch $\mathbf{P}_r$. We define a set $Q_r \subset X$ as

$$Q_r \equiv \{x \in X : \ \underline{b}_r \leq d(\mathbf{P}_x - \mathbf{P}_r)/\sigma^2 \leq \bar{b}_r\}, \tag{2.2}$$

where $d(\mathbf{P}_x - \mathbf{P}_r)$ denotes the Euclidean distance between patches $\mathbf{P}_x$ and $\mathbf{P}_r$, and $\underline{b}_r$, $\bar{b}_r$ are parameters controlling size of the two-sided confidence interval Q_r testing the hypothesis that $\mathbf{P}_x$ and $\mathbf{P}_r$ are noisy versions of underlying close clean patches.

Assuming that the clean patches are identical the distance $d(\mathbf{P}_x - \mathbf{P}_r)$ has a $\chi^2(2(N_1 \times N_2))$. For large $N_1 N_2$ this χ^2 distribution is well approximated by Gaussian with mean and variance equal to $2N_1N_2\sigma^2$ and $4N_1N_2\sigma^4$, respectively. We define the lower and upper bounds in (2.2) as $\underline{b}_r = \max(0, 2N_1N_2 - q_1 2\sqrt{N_1N_2})$ and $\underline{b}_r = 2N_1N_2 + q_1q_2 2\sqrt{N_1N_2}$, where q_1 is a Gaussian distribution quantile. We take $q_1 = 3$ (three sigma rule) and assume that $q_2 > 1$ in $\bar{b}_r$ in order to extend the confidence interval beyond a size obtained under the hypothesis that the clean patches in $\mathbf{P}_x$ and $\mathbf{P}_r$ are identical.

The matched noisy patches $\mathbf{P}_x$, for $x \in Q_r$ are stacked to form a 3D array of size $N_1 \times N_2 \times J_r$, denoted by $\mathbf{Z}^r$, where J_r denotes a length of the array (the number of elements in Q_r)

2. **HOSVD**

The 3D group $Z^r \subset \mathbb{C}^{N_1 \times N_2 \times J_r}$ can be treated as a tensor of the dimension $N_1 \times N_2 \times J_r$. The elements of this tensor can be expressed as $\mathbf{Z}^r_{l_1,l_2,l_3}$with $l_1 = 1, ..., N_1$, $l_2 = 1, ..., N_2$ and $l_3 = 1, ..., J_r$. In order to treat the group $\mathbf{Z}^r$ as a whole $3D$ entity, techniques on the multilinear algebra can be used in order to take into account correlations inside and between patches. It is well known that SVD (singular value decomposition) is important for matrix analysis. Similarly, there are a number of various tensor decompositions as the most important ones we mention TUCKER3 and PARAFAC [16] - [18].

In this paper we use the HOSVD (TUCKER3) transform allowing to represent the group-tensor in the form

$$\mathbf{Z}^r = \mathbf{S}^r \times_1 \mathbf{T}_{1,r} \times_2 \mathbf{T}_{2,r} \times_3 \mathbf{T}_{3,r}, \tag{2.3}$$

where $\mathbf{T}_{1,r} \subset \mathbb{C}^{N_1 \times N_2}$, $\mathbf{T}_{2,r} \subset \mathbb{C}^{N_1 \times N_2}$ and $T_{3,r} \subset \mathbb{C}^{N_{J_r} \times N_{J_r}}$ are orthonormal transform matrices, $\mathbf{S}^r \in \mathbb{C}^{N_1 \times N_1 \times J_r}$ is the so-called *core tensor*, and symbols $\times_1$, $\times_2$, $\times_3$ stand for the products of the corresponding modes (variables). The matrix transform $\mathbf{T}_{1,r}$ acts with respect to the variable l_1 in $\mathbf{Z}^r_{l_1,l_2,l_3}$ provided that l_2 and l_2 are fixed, similar meaning have the mode transforms $\times_2\mathbf{T}_{2,r}$ and $\times\mathbf{T}_{3,r}$ with respect to the variables l_2 and l_3.

3. **Thresholding**

In the standard two-dimensional SVD the spectral matrix is diagonal composed from non-negative singular values of the matrix to be analyzed and the transform matrices are real-valued. Usually, a number of large singular values is small and data filtering is produced by zeroing the elements of the diagonal spectral matrix which are smaller some threshold. These truncated SVD based approximations have been extensively used in signal and image processing both to carry out denoising and to obtain low rank approximation of the original matrices.

HOSVD applied to the complex-valued data gives the complex-valued orthonormal transform matrices $\mathbf{T}_{1,r}$, $\mathbf{T}_{2,r}$ $\mathbf{T}_{3,r}$ and a complex-valued core tensor $\mathbf{S}^r$. However, as show the experiments, in our tests, a small number of tensor components with large energy (absolute values) dominate the group representation. Thus, assuming that smaller elements of $\mathbf{S}^r$ are linked to noise and not to essential components of

the signal, the element wise thresholding for filtering of $\mathbf{S}^r$ is used in the form

$$\hat{\mathbf{S}}^r = \text{thresh}(\mathbf{S}^r, \delta_r), \tag{2.4}$$

where thresh$(\cdot)$ stands for the hard-/soft-threshold function.

Specific features of the thresholding function for the complex domain are studied in Section 3, where this function is derived as an optimal solution for some optimization problem.

As per rule derived in [23] we select as the universal threshold

$$\delta_r = \eta\sigma\sqrt{2\log N_1 N_2 J_r}, \tag{2.5}$$

where η parameter of the algorithm is selected from experiments.

After the thresholding the filtered group data are reconstructed using the formula (2.3) as

$$\hat{\mathbf{U}}^r = \hat{\mathbf{S}}^r \times_1 \mathbf{T}_{1,r} \times_2 \mathbf{T}_{2,r} \times \mathbf{T}_{3,r}. \tag{2.6}$$

4. **Aggregation and wavefield reconstruction**

After the thresholding step, each of the $3D$ arrays $\hat{\mathbf{U}}^r$, for $r \in X$, contains J_r stacked local patch estimates $\mathbf{P}_{x\in Q_r}$ of the corresponding true patches.

We remark that due to the patch overlapping and grouping process, the set of patches contained in the 3D groups Q_r, for $r \in X$, provides an overcomplete representation of the estimated image u. Define $\hat{u}_{r,y}(x)$ as the estimate of $u(x)$ provided by patch y if $y \in Q_r$ and $x \in \mathcal{P}_y$ and $\hat{u}_{r,y}(x) = 0$ otherwise. With these definition in place, we compute the aggregated estimate of $u(x)$ as the weighted mean

$$\hat{u}(x) = \frac{\sum_{r\in X} g_r \sum_{y\in Q_r} \hat{u}_{r,y}(x)}{\sum_{r\in X} g_r \sum_{y\in Q_r} \mathcal{I}_{\mathcal{P}_y}(x)}, \tag{2.7}$$

where $\mathcal{I}_{\mathcal{P}_y}(x)$ stands for the indicator of set $\mathcal{P}_y$.

The weights g_r are calculated as

$$g_r = 1/\chi(\hat{\mathbf{S}}^r) \tag{2.8}$$

$\chi(\hat{\mathbf{S}}^r)$ is the cardinality number of $\hat{\mathbf{S}}^r$, i.e. the number of active (non-zero) elements of the core tensor $\hat{\mathbf{S}}^r$ after thresholding.

The total power of noise in the core tensor is proportional to the cardinality number. Thus, the weighted mean (2.7) uses inverse variances for aggregation of multiple estimates.

If we take $g_r = 1$ for all r, the denominator of (2.7) is always greater or equal to 1 because all image pixels are covered at least by a patch. In practice, for most pixels we have $\sum_{r\in X} \sum_{y\in Q_r} \mathcal{I}_{\mathcal{P}_y}(x) \gg 1$ because a patch containing x was cooperatively used in many groups.

When $\hat{u}(x)$ is calculated reconstruction of amplitude and interferometric phase is of the form

$$\hat{a} = abs(\hat{u}(x)),\ \hat{\varphi} = \arg(\hat{u}(x)). \tag{2.9}$$

The input-output relation in this algorithm will be denoted as

$$\hat{u} = CD\text{-}BM3D(z, \delta), \tag{2.10}$$

where δ stands for the thresholding parameter.

2.2. Overcomplete spectral representations and CD-BM3D. Let $\mathbf{u} \in \mathbb{C}^n$ be a vectorized representation of the complex-valued object $u(x)$ in (2.1). Denote $\mathbf{a} = \text{abs}(\mathbf{u})$ and $\boldsymbol{\varphi} = \text{angle}(\mathbf{u}) \in [-\pi, \pi)$ as, respectively, the corresponding images of amplitude (modulus) and interferometric phase, $\boldsymbol{\varphi}$. Then we have $\mathbf{u} = \mathbf{a} \circ \exp(j\boldsymbol{\varphi})$. In the vectorized representations all functions applied to vectors are to be understood in the component-wise sense; the same applies to multiplications of vectors (denoted as '$\circ$').

With the objective of formulating treatable phase imaging problems, most approaches follow a two-step procedure: in the first step, an estimate of the so-called interferometric (principal, wrapped) phase in the interval $[-\pi, \pi)$ is determined; in the second step, termed phase unwrapping, the absolute phase is inferred by adding of an integer number of 2π multiples to the estimated interferometric phase [24]. In what follows, we denote the interferometric phase as $\boldsymbol{\varphi}$ and the absolute phase as $\boldsymbol{\varphi}_{abs}$. We introduce the phase-wrap operator $\mathcal{W} : \mathbb{R} \mapsto [-\pi, \pi)$, linking the absolute and interferometric phase as $\boldsymbol{\varphi} = \mathcal{W}(\boldsymbol{\varphi}_{abs})$. We also define the unwrapped phase as $\boldsymbol{\varphi}_{abs} = \mathcal{W}^{-1}(\boldsymbol{\varphi})$. Note that $\mathcal{W}^{-1}$ is not an inverse operator for $\mathcal{W}$ because the latter is highly non-linear and for $2D$ images there is no one-to-one relation between $\boldsymbol{\varphi}_{abs}$ and $\boldsymbol{\varphi}$.

Let us introduce a complex domain sparse representation for $u(x)$ in the form

$$\mathbf{u} = \boldsymbol{\Psi}_{\mathbf{u}} \boldsymbol{\theta}_{\mathbf{u}}, \ \boldsymbol{\theta}_{\mathbf{u}} = \boldsymbol{\Phi}_{\mathbf{u}} \mathbf{u}, \tag{2.11}$$

where $\mathbf{u} \in \mathbb{C}^n$ and $\boldsymbol{\theta}_{\mathbf{u}} \in \mathbb{C}^p$ are complex-valued object and complex-valued object spectrum, respectively.

Herein, the syntheses $\boldsymbol{\Psi}_{\mathbf{u}}$ and analysis $\boldsymbol{\Phi}_{\mathbf{u}}$ matrices (transforms, dictionaries) for $\mathbf{u}$ are also complex-valued. Following the sparsity rationale it is assumed that the spectrum $\boldsymbol{\theta}_{\mathbf{u}}$ is sparse; i.e., most elements thereof are zero. In order to quantify the level of sparsity of $\boldsymbol{\theta}_{\mathbf{u}}$, i.e., its number of non-zero (active) elements, we use the pseudo l_0-norm $\|\cdot\|_0$ defined as a number of non-zero elements of the vector-argument. Therefore, in the ensuing formulations, we design estimation criteria promoting low values of $\|\boldsymbol{\theta}_{\mathbf{u}}\|_0$.

Usually, the spectral representations are highly overcomplete with $p \gg n$, while the number of the active elements, i.e. the pseudo l_0-norms of spectra, are much smaller than p.

We wish to install a correspondence between sparsity modeling in the form (2.11) and CD-BM3D introduced in Subsection 2.1.

For given BM3D's groups $\{Q_r\}$ and HOSVD transforms $\{\mathbf{T}_{1,r}, \mathbf{T}_{2,r}, \mathbf{T}_{3,r}\}$ calculated for all groups the link between the observation $z(x)$, $x \subset X$, and HOSVD spectra $\{\mathbf{S}^r\}$ is linear and can be given as

$$\boldsymbol{\theta}_{\mathbf{z}} = \boldsymbol{\Phi}_{\mathbf{z}} \mathbf{z}, \tag{2.12}$$

where $\mathbf{z} \in \mathbb{C}^n$ is an observation vector corresponding to (2.1), $\boldsymbol{\theta}_{\mathbf{z}} \in \mathbb{C}^p$ is a vector composed from all items of $\{\mathbf{S}^r\}$ and the transform matrix $\boldsymbol{\Phi}_{\mathbf{z}}$ is defined by BM3D grouping and HOSVD operations.

Comparing with (2.11) we may interpret (2.12) as the analysis transform defined by the steps 1 and 2 of CD-BM3D and applied to the noisy observation.

A synthesis transform, another linear operation in CD-BM3D, is defined by inverse HOSVD and aggregation step 4 of CD-BM3D. This operation can be presented in the form

$$\hat{\mathbf{u}} = \boldsymbol{\Psi}_{\mathbf{z}} \hat{\boldsymbol{\theta}}_{\mathbf{z}}, \tag{2.13}$$

where $\hat{\boldsymbol{\theta}}_{\mathbf{z}}$ is a vector of the thresholded (filtered) components of the spectrum $\boldsymbol{\theta}_{\mathbf{z}}$, $\hat{\mathbf{u}}$ is the vectorized estimate $\hat{u}(x)$ and $\boldsymbol{\Psi}_{\mathbf{z}}$ is a synthesis transform matrix.

Therefore, the introduced analysis and synthesis transforms allow to represent CD-BM3D in the compact form:

$$\boldsymbol{\theta}_{\mathbf{z}} = \boldsymbol{\Phi}_{\mathbf{z}}\mathbf{z},\ \hat{\boldsymbol{\theta}}_{\mathbf{z}} = \mathrm{thresh}(\boldsymbol{\theta}_{\mathbf{z}}, \delta),\ \hat{\mathbf{u}} = \boldsymbol{\Psi}_{\mathbf{z}}\hat{\boldsymbol{\theta}}_{\mathbf{z}}. \tag{2.14}$$

The real domain BM3D as it in [15] is different from CD-BM3D by using the same fixed transforms $\mathbf{T}_{1,r}$, $\mathbf{T}_{2,r}$, $\mathbf{T}_{3,r}$ for each group. It gives opportunity to go much further in the study of the corresponding sparse representation (2.11). It is shown in [25] that $\boldsymbol{\Phi}_{\mathbf{z}}$ and $\boldsymbol{\Psi}_{\mathbf{z}}$ are non-tight frames (named BM3D frames). Moreover, if $g_r = 1$, $\boldsymbol{\Psi}_{\mathbf{z}} = \mathbf{W}^{-1}\boldsymbol{\Phi}_{\mathbf{z}}^H$, where $\mathbf{W}$ is a diagonal matrix with integers indicating number of groups where the corresponding pixel is used.

This statement cannot be extended for CD-BM3D, where the transforms $\{\mathbf{T}_{1,r}$, $\mathbf{T}_{2,r}$, $\mathbf{T}_{3,r}\}$ generated by HOSVD are different for each group. Nevertheless, it can be seen that $\boldsymbol{\Psi}_{\mathbf{z}}\boldsymbol{\Phi}_{\mathbf{z}} = \mathbf{I}_{n\times n}$ for CD-BM3D. Thus, provided no thresholding, $\hat{\boldsymbol{\theta}}_{\mathbf{z}} = \boldsymbol{\theta}_{\mathbf{z}}$, the perfect reconstruction of the input signal is guaranteed, $\hat{\mathbf{u}} = \boldsymbol{\Psi}_{\mathbf{z}}\boldsymbol{\Phi}_{\mathbf{z}}\mathbf{z} = \mathbf{z}$.

The representation of CD-BM3D in the form (2.14) is exploited further for derivation of an iterative version of this algorithm. Note, that in implementation of CD-BM3D the transform-matrices $\boldsymbol{\Phi}_{\mathbf{z}}$ and $\boldsymbol{\Psi}_{\mathbf{z}}$ are not calculated and passages from $\mathbf{z}$ to $\boldsymbol{\theta}_{\mathbf{z}}$ and from $\hat{\boldsymbol{\theta}}_{\mathbf{z}}$ to $\hat{\mathbf{u}}$ are defined algorithmically.

3. Sparse modeling of complex exponent.

3.1. Variational formulation. Two different variational formulations classified as the analysis and synthesis approaches can be viewed for sparse modeling. Specifically, in the *synthesis* approach the variational setup for the Gaussian observations (2.1) is of the form

$$\min_{\boldsymbol{\theta}_{\mathbf{u}}} ||\boldsymbol{\theta}_{\mathbf{u}}||_p \text{ s.t. } ||\mathbf{z} - \boldsymbol{\Psi}_{\mathbf{u}}\boldsymbol{\theta}_{\mathbf{u}}||_2^2 < \varepsilon, \tag{3.1}$$

where $\boldsymbol{\Psi}_{\mathbf{u}}\boldsymbol{\theta}_{\mathbf{u}}$ means an estimate for $\mathbf{u}$, $\varepsilon > 0$, and $||\boldsymbol{\theta}_{\mathbf{u}}||_p$ can be $\|\boldsymbol{\theta}_u\|_0$ or $\|\boldsymbol{\theta}_u\|_1$.

The pseudo-norm l_0, $\|\boldsymbol{\theta}_u\|_0$, is calculated as a number of nonzero elements of vector $\boldsymbol{\theta}_{\mathbf{u}}$. Aiming at optimal sparse representation and thus at optimal noise removing minimization of l_0 is a straightforward idea in sparse modeling. The norm l_1, $\|\boldsymbol{\theta}_u\|_1$, is a sum of absolute values of the elements of vector $\boldsymbol{\theta}_{\mathbf{u}}$. In sparse imaging the l_1-norm is used as a convex replacement for the non-convex l_0 with an intention to reformulate optimization as a convex problem.

An elaborated theory and algorithms are strong arguments in favor of convexity for optimization. On some occasions in sparse imaging the solutions given by l_0 and l_1 are close to each other. Both l_0 and l_1 are standard attributes of variational settings supporting sparsity.

The problem (3.1) is a constrained optimization provided a quadratic norm restriction due to Gaussian random noise in observations.

The alternative *analysis* approach has a different formalization:

$$\min_{\mathbf{u}} ||\boldsymbol{\Phi}_{\mathbf{u}}\mathbf{u}||_p \text{ s.t. } ||\mathbf{z} - \mathbf{u}||_2^2 < \varepsilon. \tag{3.2}$$

Here again we minimize the model complexity in the spectral domain provided quadratic restrictions in the image domain. Nevertheless, formal distinctions between these two formulations are quite obvious. In the synthesis approach minimization

is produced in the spectral domain and only the synthesis transform $\mathbf{\Psi_u}$ is used. Contrary to it, in the analysis approach minimization is in the image domain and the analysis transform $\mathbf{\Phi_u}$ is used only.

For real-valued domain a comparative study of the analysis and synthesis techniques is a topic of a number of publications and it is well known that the obtained results can be quite different [26].

Herein, we adopt a different Nash equilibrium formulation. Contrary to the analysis and synthesis approaches it uses both synthesis and analysis transforms and results in a more manageable optimization.

A single criterion constrained optimization in (3.1)-(3.2) is replaced by a search for the Nash equilibrium balancing two criteria. Motivations and details of this approach as it is applied to BM3D filtering in the real domain, links with the game theory and demonstration of its efficiency for the sparse inverse imaging can be seen in [25]. In what follows we adapt this Nash equilibrium technique to the complex domain formulation.

The maximum likelihood concept for the observations (2.1) and the sparsity restrictions lead to the criteria:

$$\mathcal{L}_1(\mathbf{u},\, \boldsymbol{\theta}_\mathbf{u}) = ||\mathbf{z}-\mathbf{u}||_2^2 + \frac{1}{\gamma}||\mathbf{u}-\mathbf{\Psi_u}\boldsymbol{\theta}_\mathbf{u}||_2^2, \tag{3.3}$$

$$\mathcal{L}_2(\mathbf{u},\, \boldsymbol{\theta}_\mathbf{u}) = \tau\cdot||\boldsymbol{\theta}_\mathbf{u}||_p + \frac{1}{2}||\boldsymbol{\theta}_\mathbf{u}-\mathbf{\Phi_u}\mathbf{u}||_2^2, \tag{3.4}$$

where $\gamma>0$ and $\tau>0$ are regularization parameters.

Here $\mathbf{\Psi_u}$, $\mathbf{\Phi_u}$ are synthesis and analysis transforms and $\boldsymbol{\theta}_\mathbf{u}$ stands for spectra of the complex-valued $\mathbf{u}$ as they are introduced above. The first summand in $\mathcal{L}_1(\mathbf{u},\, \boldsymbol{\theta}_\mathbf{u})$ corresponds to the minus Gaussian loglikelihood, and the second is a regularization term defined by the differences between the variables $\mathbf{u}$ and its sparse estimate $\mathbf{\Psi_u}\boldsymbol{\theta}_\mathbf{u}$.

The l_p in $\mathcal{L}_2(\boldsymbol{\theta}_\mathbf{u})$ promotes the sparsity of $\mathbf{u}$ in the spectrum domain. The second summand in $\mathcal{L}_2(\boldsymbol{\theta}_\mathbf{u},\, \boldsymbol{\theta}_\mathbf{a})$ is a quadratic regularization term defined through the differences between the spectrum variable $\boldsymbol{\theta}_\mathbf{u}$ and its analysis estimate $\mathbf{\Phi_u}\mathbf{u}$.

Following the Nash equilibrium technique balancing, in general, multiple penalty functions (e.g. [27]) we propose the algorithm composed of alternating iterations minimizing the criteria $\mathcal{L}_1$ and $\mathcal{L}_2$.

For the criteria (3.3)-(3.4) the Nash equilibrium can be pursued by iterations:

$$\begin{aligned}\boldsymbol{\theta}_\mathbf{u}^{t-1} &= \arg\min_{\boldsymbol{\theta}_\mathbf{u}} \mathcal{L}_2(\mathbf{u}^{t-1},\, \boldsymbol{\theta}_\mathbf{u}),\\ \mathbf{u}^{t} &= \arg\min_{\mathbf{u}} \mathcal{L}_1(\mathbf{u},\, \boldsymbol{\theta}_\mathbf{u}^{t-1}).\end{aligned} \tag{3.5}$$

Minimization of $\mathcal{L}_1(\mathbf{u},\, \mathbf{a})$ which is quadratic on $\mathbf{u}$ leads to the linear equation $\partial\mathcal{L}_1/\partial\mathbf{u}^*=0$ and the solution:

$$\mathbf{u} = (\mathbf{z}+\frac{1}{\gamma}\mathbf{\Psi_u}\boldsymbol{\theta}_\mathbf{u})/(1+\frac{1}{\gamma}). \tag{3.6}$$

Minimization of $\mathcal{L}_2$ on $\boldsymbol{\theta}_\mathbf{u}$ results in the complex domain element-wise thresholding of the spectrum $\mathbf{\Phi_u}\mathbf{u}$: hard-and soft-thresholding, respectively, for optimization with l_0 and l_1.

The solution of this minimization can be represented in the following form:

$$\hat{\boldsymbol{\theta}}_{\mathbf{u}} = thresh(\boldsymbol{\Phi}_{\mathbf{u}}\mathbf{u},\delta) \equiv \tag{3.7}$$
$$\begin{cases} \boldsymbol{\Phi}_{\mathbf{u}}\mathbf{u} \circ 1\left[abs(\boldsymbol{\Phi}_{\mathbf{u}}\mathbf{u}) \geq \delta\right],\ \delta = \sqrt{2\tau},\ \text{if } l_p = l_0, \\ \\ \dfrac{\boldsymbol{\Phi}_{\mathbf{u}}\mathbf{u}}{abs(\boldsymbol{\Phi}_{\mathbf{u}}\mathbf{u})} \circ \max(abs(\boldsymbol{\Phi}_{\mathbf{u}}\mathbf{u}) - \delta, 0),\ \delta = \tau,\ \text{if } l_p = l_1, \end{cases}$$

where $1[x] = 1$ if $x \geq 0$ and $1[x] = 0$ otherwise.

The thresholding parameter δ is equal to $\sqrt{2\tau}$ for l_0 and equal to τ for l_1. The items of the spectral vectors $abs(\boldsymbol{\Phi}_{\mathbf{u}}\mathbf{u})$, which are smaller than δ are zeroed in Eq.(3.7), while the interferometric phase of the complex-valued $\boldsymbol{\Phi}_{\mathbf{u}}\mathbf{u}$ is preserved for non-zero elements of $\boldsymbol{\Phi}_{\mathbf{u}}\mathbf{u}$. Overall, the thresholding manipulates the absolute values only and does not change the phase of the input. Remind that all operations with the vectorized variables are element-wise.

Let us derive the rule (3.7) from minimization of $\mathcal{L}_2$ on $\boldsymbol{\theta}_{\mathbf{u}}$. First of all note, that the criterion (3.4) can be rewritten as

$$\mathcal{L}_2(\mathbf{u}, \boldsymbol{\theta}_{\mathbf{u}}) = \tau \cdot ||\mathbf{a}_{\boldsymbol{\theta}_{\mathbf{u}}}||_p + \frac{1}{2}||\mathbf{a}_{\boldsymbol{\theta}_{\mathbf{u}}} \circ \exp(j\boldsymbol{\varphi}_{\boldsymbol{\theta}_{\mathbf{u}}}) - \mathbf{a}_{\boldsymbol{\Phi}_{\mathbf{u}}\mathbf{u}} \circ \exp(j\boldsymbol{\varphi}_{\boldsymbol{\Phi}_{\mathbf{u}}\mathbf{u}})||_2^2, \tag{3.8}$$

where $\boldsymbol{\varphi}_{\boldsymbol{\theta}_{\mathbf{u}}}$, $\boldsymbol{\varphi}_{\boldsymbol{\Phi}_{\mathbf{u}}\mathbf{u}}$ are the interferometric phases of $\boldsymbol{\theta}_{\mathbf{u}}$ and $\boldsymbol{\Phi}_{\mathbf{u}}\mathbf{u}$, respectively, and $\mathbf{a}_{\boldsymbol{\theta}_{\mathbf{u}}}$ and $\mathbf{a}_{\boldsymbol{\Phi}_{\mathbf{u}}\mathbf{u}}$ are the amplitudes of $\boldsymbol{\theta}_{\mathbf{u}}$ and $\boldsymbol{\Phi}_{\mathbf{u}}\mathbf{u}$ in the representation of $\boldsymbol{\theta}_{\mathbf{u}}$ and $\boldsymbol{\Phi}_{\mathbf{u}}\mathbf{u}$ in the form $\boldsymbol{\theta}_{\mathbf{u}} = \mathbf{a}_{\boldsymbol{\theta}_{\mathbf{u}}} \circ \exp(j\boldsymbol{\varphi}_{\boldsymbol{\theta}_{\mathbf{u}}})$, $\boldsymbol{\Phi}_{\mathbf{u}}\mathbf{u} = \mathbf{a}_{\boldsymbol{\Phi}_{\mathbf{u}}\mathbf{u}} \circ \exp(j\boldsymbol{\varphi}_{\boldsymbol{\Phi}_{\mathbf{u}}\mathbf{u}})$.

Minimization of $\mathcal{L}_2(\mathbf{u},\, \boldsymbol{\theta}_{\mathbf{u}})$ on the complex-valued $\boldsymbol{\theta}_{\mathbf{u}}$ can be produced independently on amplitude and phase of $\boldsymbol{\theta}_{\mathbf{u}}$. Minimization on $\boldsymbol{\varphi}_{\boldsymbol{\theta}_{\mathbf{u}}}$ for (3.8) immediately gives

$$\boldsymbol{\varphi}_{\boldsymbol{\theta}_{\mathbf{u}}} = \boldsymbol{\varphi}_{\boldsymbol{\Phi}_{\mathbf{u}}\mathbf{u}}. \tag{3.9}$$

Inserting this solution in (3.8) we obtain $\mathcal{L}_2$ depending only on the amplitudes:

$$\mathcal{L}_2(\mathbf{u}, \boldsymbol{\theta}_{\mathbf{u}})\big|_{\boldsymbol{\varphi}_{\boldsymbol{\theta}_{\mathbf{u}}} = \boldsymbol{\varphi}_{\boldsymbol{\Phi}_{\mathbf{u}}\mathbf{u}}} = \tau \cdot ||\mathbf{a}_{\boldsymbol{\theta}_{\mathbf{u}}}||_p + \frac{1}{2}||\mathbf{a}_{\boldsymbol{\theta}_{\mathbf{u}}} - \mathbf{a}_{\boldsymbol{\Phi}_{\mathbf{u}}\mathbf{u}}||_2^2. \tag{3.10}$$

It can be verified that minimization of $\mathcal{L}_2(\mathbf{u}, \boldsymbol{\theta}_{\mathbf{u}})\big|_{\boldsymbol{\varphi}_{\boldsymbol{\theta}_{\mathbf{u}}} = \boldsymbol{\varphi}_{\boldsymbol{\Phi}_{\mathbf{u}}\mathbf{u}}}$ on real-valued $\mathbf{a}_{\boldsymbol{\theta}_{\mathbf{u}}}$ gives the standard hard- and soft-thresholding functions:

$$a_{out} = f(a_{in},\, \delta) \equiv \begin{cases} a_{in} \times 1[|a_{in}| \geq \sqrt{2\tau}],\ \text{if } l_p = l_0, \\ \\ sign\,(a_{in}) \times \max\left(|a_{in}| - \tau, 0\right),\ \text{if } l_p = l_1, \end{cases} \tag{3.11}$$

where a_{in} and a_{out} are elements of the amplitude vectors $\mathbf{a}_{\boldsymbol{\Phi}_{\mathbf{u}}\mathbf{u}}$ and $\mathbf{a}_{\boldsymbol{\theta}_{\mathbf{u}}}$, respectively.

For the complex valued $x_{in} = a_{in}\exp(j\varphi_{in})$ and $x_{out} = a_{out}\exp(j\varphi_{out})$ due to (3.9) $\varphi_{in} = \varphi_{out}$ and we obtain from (3.11)

$$x_{out} = thresh(x_{in},\, \delta) \equiv \begin{cases} x_{in} \times 1[abs(x_{in}) \geq \sqrt{2\tau}],\ \text{if } l_p = l_0, \\ \\ \dfrac{x_{in}}{abs(x_{in})} \times \max\left(abs(x_{in}) - \tau, 0\right),\ \text{if } l_p = l_1, \end{cases}, \tag{3.12}$$

where x_{in} and x_{out} are elements of the complex-valued vectors $\boldsymbol{\Phi}_{\mathbf{u}}\mathbf{u}$ and $\boldsymbol{\theta}_{\mathbf{u}}$, respectively.

It is useful to note here that in representation of complex-valued x in the form $x = a_x \exp(j\varphi_x)$ the amplitude a_x may take positive and negative values. Contrary to it in the representation $x = abs(x)\exp(j\tilde{\varphi}_x)$ the amplitude $abs(x) \geq 0$ and the sign of a_x is translated in the phase $\tilde{\varphi}_x$ by including summand π if $a_x < 0$. In the derivation of (3.12) we use $a_{x_{in}}/sign(a_{x_{in}}) = abs(a_{x_{in}}) = abs(x_{in})$.

The formula (3.7) to be proved is a vectorized version of (3.12) applied to a vectorial input.

3.2. Iterative CD-BM3D. Let us use CD-BM3D transforms as the analysis and synthesis operators for iterations (3.5). These analysis and synthesis transforms are complex-valued obtained through HOSVD applied to non-local BM3D groups.

It follows from (2.14) that $\mathbf{\Psi_u \theta_u}$, where $\boldsymbol{\theta}_\mathbf{u} = thresh(\mathbf{\Phi_u u}, \delta)$, is the output of the CD-BM3D filter for the input $\mathbf{u}$, provided a given grouping. The estimates of $\mathbf{u}$ and $\boldsymbol{\theta}_\mathbf{u}$ are calculated according to (3.6)-(3.7). Using these estimates in the iterations (3.5) we arrive to the algorithm shown in Table I.

TABLE 3.1
ITERATIVE CD-BM3D.

	Input: z;
1	*Initialization:* $u^0 = z$;
	Iterations for $t = 1, .., K$;
2	$v^t = u^{t-1} + \alpha(z - u^{t-1})$;
3	$u^t = CD\text{-}BM3D(v^t, \delta)$;
4	*end*
	Output: u^K.

In Table I all variables are shown for 2D complex domain $\mathbb{C}^2$, what makes the formulas simpler and different from those in (3.6)-(3.7), where the estimates are presented in the vectorized form.

In this presentation of the algorithm we replace the parameter γ by $\alpha = 1/(1 + 1/\gamma)$, $0 < \alpha < 1$ for $\gamma > 0$.

It is not difficult to realize that for any α the first iteration of this algorithm gives $u^1 = CD\text{-}BM3D(z, \delta)$ as an output of the CD-BM3D algorithm with the observation z as the input.

According to Step 2 the estimate update is calculated as the sum of the previous estimate and the deviation of this estimate from the observation z. The step size α defines a magnitude of observation noise in the update. This update is filtered at Step 3 of the algorithm.

The free parameters of this algorithm are α and δ. It is typical to use the algorithms derived from the variation formulation similar to (3.3)-(3.4) with varying parameter α_t, δ_t, such that α_t, $\delta_t \to 0$.

3.3. Convergence of iterative CD-BM3D. The iterative CD-BM3D (Table I) can be rewritten as a single line

$$u^t = CD\text{-}BM3D(u^{t-1} + \alpha(z - u^{t-1}), \delta). \tag{3.13}$$

A fixed or steady-state point of the algorithm $\tilde{u}$ is a solution of the equation

$$\tilde{u} = CD\text{-}BM3D(\tilde{u} + \alpha(z - \tilde{u}), \delta). \tag{3.14}$$

PROPOSITION 3.1. *Let CD-BM3D be a nonexpansive operator satisfying the Lipschitz condition:*

$$||u^1 - u^2||_F \le k_\delta ||z^1 - z^2||_F,\ z^1,\ z^2 \subset \mathbb{C}^{\sqrt{n}\times\sqrt{n}}, \qquad (3.15)$$
$$0 \le k_\delta \le 1,$$

where $u^1 = CD\text{-}BM3D(z^1, \delta)$, $u^2 = CD\text{-}BM3D(z^2, \delta)$ *and* $||\cdot||_F$ *stands for the Frobenius norm.*

Then, the fixed-point equation (3.14) has an uniqueness solution and the iterative CD-BM3D algorithm converges to this solution with a geometric convergence rate

$$||u^t - \tilde{u}||_F \le q||u^{t-1} - \tilde{u}||_F\,, \qquad (3.16)$$
$$q = (1-\alpha)k_\delta < 1.$$

Proof. Let us assume that there are two different solutions of (3.14) $\tilde{u}^1$ and $\tilde{u}^2$. For the difference of these solutions we obtain due to (3.14) and (3.15)

$$||\tilde{u}^1 - \tilde{u}^2||_F = ||CD\text{-}BM3D(\tilde{u}^1 + \alpha(z - \tilde{u}^1), \delta) - \qquad (3.17)$$
$$CD\text{-}BM3D(\tilde{u}^2 + \alpha(z - \tilde{u}^2), \delta)||_F \le$$
$$q||\tilde{u}^1 - \tilde{u}^2||_F.$$

Iterations of the last inequality show that $||\tilde{u}^1 - \tilde{u}^2||_F \le q^k||\tilde{u}^1 - \tilde{u}^2||_F$, for any integer $k > 0$. Then, $||\tilde{u}^1 - \tilde{u}^2||_F \to 0$ as $k \to \infty$, i.e. there are no two different solutions. It proves by contradiction the uniqueness of the fixed-point solution.

Further, consider difference between u^t and $\tilde{u}$. Calculations similar to (3.17) show that $||u^t - \tilde{u}||_F \le q||u^{t-1} - \tilde{u}||_F$. By contradiction, it proves (3.16) and defines the convergence rate parameter q. □

It is obvious from the proof that actually the proposition is a consequence of the Lipschitz condition (3.15). The algorithm CD-BM3D has a sophisticated nonlinear structure with an imbedded combinatorial patch-wise grouping and data dependent HOSVD transforms different for each group. Thus, it is hard to expect that the Lipschitz condition can be proved for this type of the algorithms.

We treat the Lipschitz condition (3.15) as a fruitful conjecture and validated it empirically by extensive experimental study produced for various types of input complex domain images and different parameters of CD-BM3D.

The following four scenarios of these experiments should be mentioned.

I). The input complex exponents are random $z^1 = |a_1(x)|e^{j\varphi_1(x)}$ and $z^2 = |a_2(x)|e^{j\varphi_2(x)}$, where $a_1(x)$, $a_2(x)$, $\varphi_1(x)$ and $\varphi_2(x)$ are zero-mean $2D$ Gaussian. We considered these random amplitudes and phases with correlation on x varying from i.i.d. to strongly correlated ones. This correlation was enforced by $2D$ convolution of the i.i.d. Gaussian random $a_1(x)$, $a_2(x)$, $\varphi_1(x)$ and $\varphi_2(x)$ with uniform smoothing kernels of different width.

The Lipshitz parameter k_δ is calculated as

$$k_\delta = ||u^1 - u^2||_F / ||z^1 - z^2||_F. \qquad (3.18)$$

For all experiments and for various threshold parameters of CD-BM3D the results for (3.18) confirm that $k_\delta \le 1$.

2). The input signals z^1 and z^2 are noisy object images u^1 and u^2, respectively, with the object complex exponents used in our experiments in Section 4.2.1.

In Figs.3.1 and 3.2 we show the estimates of the Lipshitz parameter k_δ obtained for the five test-images from Section 4.2.1 provided that $u^1 = u^2$ and $\sigma = .1$ and $\sigma = .9$. In these figures each curves corresponds to one of the test-images. We do not specify relations between the curves and the test-images as only a qualitative behavior of the curves is of the interest.

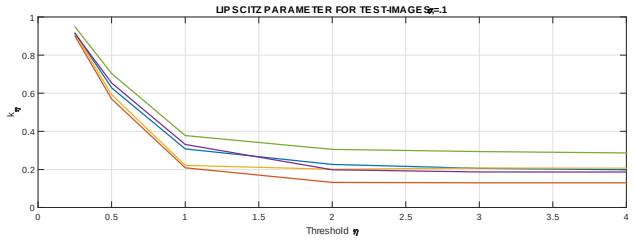

FIG. 3.1. *The estimates of the Lipschitz parameter as a function of the threshold parameter η in (2.5), $\sigma = .1$.*

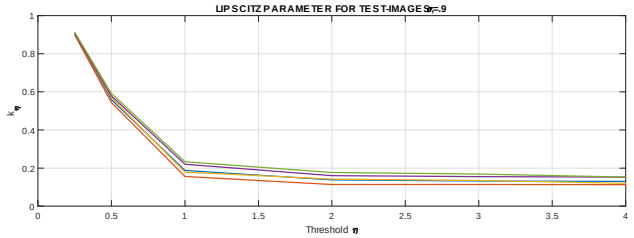

FIG. 3.2. *The estimates of the Lipschitz parameter as a function of the threshold parameter η in (2.5), $\sigma = .9$.*

In these images k_δ is given versus the threshold parameter η in (2.5). First, all $k_\delta < 1$ and they are monotonically decreasing up to some limits as the threshold grows. The behavior of the curves is quite similar for $\sigma = .1$ and $\sigma = .9$.

3) Let in the scenario 2) the objects u^1 and u^2 be different in any pair-wise combination of the tested five images. Then, for the high level noise, $\sigma = 0.9$, $k_\delta \leq 1$ and close to 1, for various threshold values.

For the lower value of σ, $\sigma = 0.1$, $k_\delta < 1$ and it is decreasing for larger thresholds. However, this decreasing is much slower than it is in Figs.3.1-3.2.

4) In this scenario one of the input signals is u^t defined by the algorithm iterations and the second one is the fixed point $\tilde{u}$ of these iterations. The Lipschitz parameter is estimated as

$$k_\delta^t = ||CD\text{-}BM3D(\tilde{u}, \delta) - CD\text{-}BM3D(u^t, \delta)||_F / ||\tilde{u} - u^t||_F. \tag{3.19}$$

In this case we calculate the estimates k_δ^t varying in iterations t and defined on the trajectories of the algorithm's iterations. The examples of this kind of curves for k_δ^t are shown in Fig.3.3. These curves are obtained for the truncated Gaussian phase test-image (Section 4.2.1) and a set of noise variances σ^2.

We may conclude that $k_\delta^t < 1$. Lower σ^2 results in uniformly higher values of k_δ^t. In iterations, k_δ^t are decreasing as t grows and converge to some invariant values. These results demonstrate that the convergence rate as defined in (3.16) is improving in iterations as $t \to \infty$.

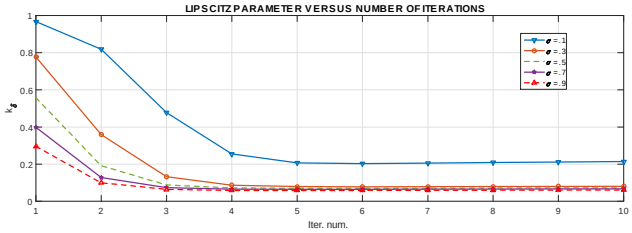

FIG. 3.3. *The estimates of the Lipschitz parameter calculated on trajectories of the iterative CD-BM3D.*

The curves in Figs.3.1-3.3 are obtained for CD-BM3D equipped with the hard-thresholding for filtering. Experiments produced for CD-BM3D with the soft-thresholding systematically show low values for the Lipshitz parameter.

4. Simulation experiments. In this section, we present simulation results illustrating effectiveness of the developed CD-BM3D algorithms in the basic and iterative versions. Based on the true interferometric phase φ and on the interferometric phase estimate $\hat{\varphi} = angle(\hat{u})$ we define the peak signal-to-noise ratio (PSNR) for the phase as

$$PSNR_{\varphi} = 10 \log_{10} \frac{4n\pi^2}{||\mathcal{W}(\hat{\varphi} - \varphi)||_F^2} [dB], \tag{4.1}$$

where n is the image size and the wrapping operator $\mathcal{W}$ is used in order to eliminate the phase-shift error multiple to 2π.

We unwrap the estimated interferometric phase with the PUMA algorithm [30] in order to get estimates of the true absolute phase φ_{abs}. The accuracy for the absolute phase reconstruction is evaluated by root-mean-square-error (RMSE):

$$RMSE_{\varphi_{abs}} = \sqrt{\frac{1}{n}||(\hat{\varphi}_{abs} - \varphi_{abs} - \Delta_{\varphi})||_F^2}, \tag{4.2}$$

where a scalar Δ_{φ} compensates a invariant shift in the absolute phase estimation due to the estimation procedure. This Δ_{φ} is calculated as the mean of the difference $\hat{\varphi}_{abs} - \varphi_{abs}$.

The reconstruction accuracy for the true amplitude a is characterized by $PSNR$:

$$PSNR_{ampl} = 10 \log_{10} \frac{n \max^2(a)}{||a - \hat{a}||_F^2} [dB], \tag{4.3}$$

where $\hat{a} = abs(\hat{u})$ is an estimate of amplitude.

In our experiments a comparison of the hard-thresholding versus the soft-thresholding in CD-BM3D is definitely in favor of the hard-thresholding. It is why all results demonstrated in this section are obtained by CD-BM3D with the hard-thresholding.

The developed CD-BM3Ds are compared with the SpInPhase algorithm [21] and Window Fourier Transform (WFT) [28], [29]. The author's codes of these algorithms are publicly available [1],[2]. The SpInPhase algorithm is applied in the internal dictionary learning mode using for estimation only noisy data in order to have a fair

[1] http://www.lx.it.pt/~bioucas/publications.html
[2] WFT-WFT-http://www.mathworks.fr/matlabcentral/fileexchange/24892

comparison versus the CD-BM3Ds. In WFT the windowed Fourier transform of z is calculated and hard thresholded. The inverse windowed Fourier transform is applied in order to obtain the estimates of φ and a. The WFT estimates were obtained with the following parameters: size of the windows $\sigma_x = \sigma_y = 4$; threshold for the windowed Fourier transform $th = 3\sigma$; frequency interval $[-\pi, \pi]$; and sampling interval 0.1. This setting was determined experimentally in [21] aiming at optimal performance for the set of the phase test images considered in Subsection 4.2.1. Remark that this setting yields considerable better results than that recommenced in [28] (i.e., $\sigma_x = \sigma_y = 4$ and $[-\pi/2, \pi/2]$). We use SpInPhase and WFT for comparison as the current state-of-the-art for the interferometric phase reconstruction. Both these algorithms operate in complex domain.

In our MATLAB implementation of CD-BM3Ds we use the tool box *tptool090831* for HOSVD transform [3] and the PUMA algorithm for phase unwrapping [30][4].

The simulation experiments are produced on a personal computer: Intel Core i7-4800 CPU@2.70 GHz and 32.00 GB RAM. All results presented in this section can be reproduced by running the publicly available MATLAB demo-codes including also the codes of the SpInPhase and WFT algorithms [5].

4.1. Parameters of CD-BM3D algorithms. We use two groups of test-images for phase: 1) piece-wise smooth absolute phase and 2) "*natural*" images (cameraman, Lena) with intrinsic geometrical structures. For the first group we reconstruct both interferometric and absolute phase while for the second group we reconstruct interferometric phase only. The second group of images is too complex for existing phase unwrapping algorithms and, practically, the unwrapping for this type of images is impossible even for noiseless data. Thus, only the wrapped phase can be reconstructed for "*natural*" images. In our modeling in order to preserve these test-images from disruption by wrapping in observation (2.1) we scaled phase to the interval $[0, \pi/4]$ radians.

For the parameters of CD-BM3D defining the grouping we follow the conventional setup of the standard BM3D: the patch size 8×8, the maximum group length is bounded by 32 and the step size between the groups is equal to 3.

Some parameters of the algorithms are different for the two groups of images. In experiments with the first group of the test-images: for CD-BM3D, the threshold parameter $\eta = 1.8$, with exclusion $\eta = 2.7$ for $\sigma = 0.1$, and for iterative CD-BM3D, $\eta = 1$, with exclusion $\eta = 2$ for $\sigma = 0.1$, and $\alpha = 0.6$ for $\sigma < 0.5$ and $\alpha = 0.56$ for $\sigma \geq 0.5$. Remind that the parameter η is linked with the threshold δ according to (2.5).

For the second group of the test-images CD-BM3D is used with the threshold parameter $\eta = 1.1$. In iterative CD-BM3D the parameters η and α are varying in iterations according to the rule $\eta^t = \mu\eta^{t-1}$ and $\alpha^t = \mu\alpha^{t-1}$, where $\eta^0 = 0.7$, $\alpha^0 = 0.65$ and $\mu = 0.98$. With these parameters 5 iterations of this algorithm suffice the convergence. In what follows the iteration number is always equal to 5.

4.2. Performance evaluation.

4.2.1. Piece-wise smooth absolute phase images. The results are given for the observation model (2.1) with the following set of the absolute phase images: trun-

[3] tptool-090831- http://www.tp-control.hu/index.php/About

[4] PUMA-http://www.lx.it.pt/~bioucas/code.htm

[5] http://www.cs.tut.fi/~lasip/DDT/index3.html

cated Gaussian, shear plane, sinusoidal continuous, sinusoidal discontinuous, mountains (for these surfaces see Fig.4.2). The amplitude $a(x) = 1$.

The true, noisy and iterative CD-BM3D interferometric phase images are demonstrated in Fig.4.1. The noisy data and reconstructions are given for the high level of the additive noise with $\sigma = 0.9$. It is clear from the middle row of these images that the degradation of the interferometric phase due to the noise is very strong. Nevertheless, the reconstructions (last row in Fig.4.1) show quite clear images close to the true ones.

The corresponding absolute phases (true and reconstructions) can be seen in Fig.4.2. Each small double-image shows both the true (left) and reconstructed absolute phase (right). The degradation of reconstruction due to the noise is well seen in the truncated Gaussian and nearly invisible for other test-images.

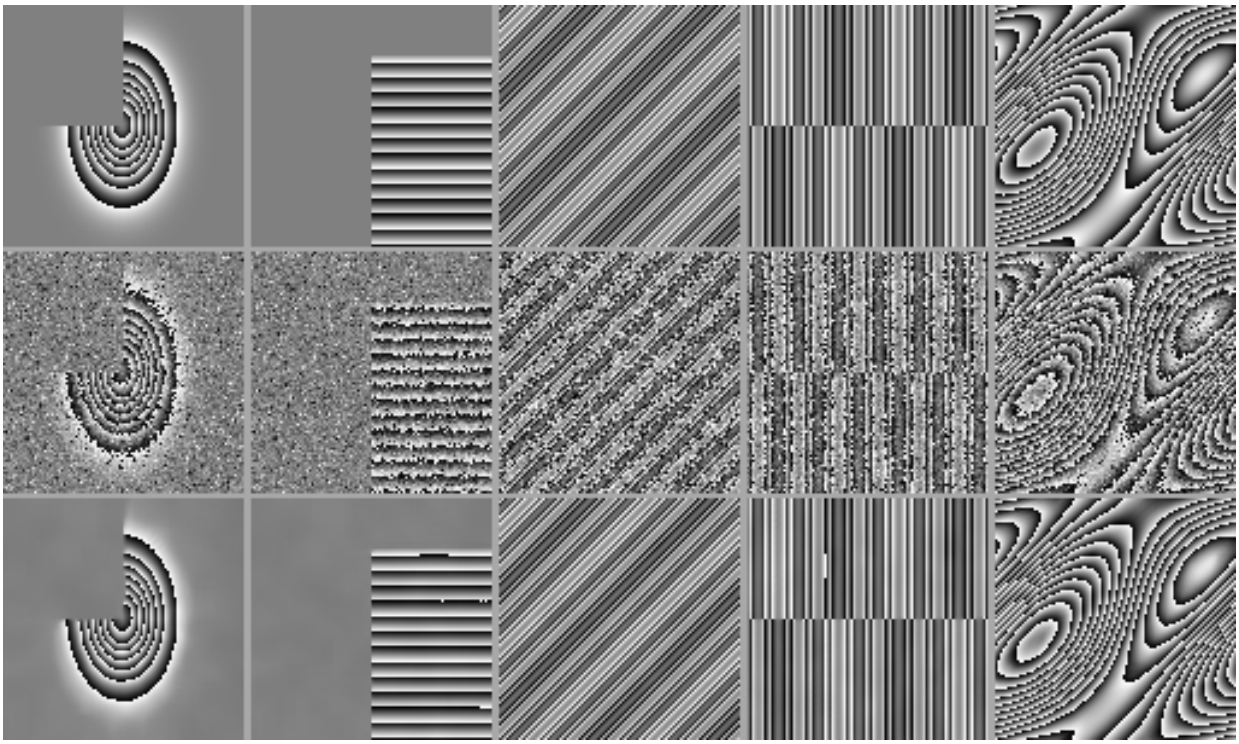

FIG. 4.1. *(From left to right) Truncated Gaussian, shear planes, continuous sinusoidal, discontinuous sinusoidal, mountains. (From top to bottom) True, noisy ($\sigma = 0.9$) and interferometric phase images reconstructed by iterative CD-BM3D.*

The accuracy of reconstruction is detailed in Table 4.1. Here we can see the columns: PSNR_{φ} for interferometric phase, $\mathrm{RMSE}_{\varphi_{abs}}$ for absolute phase and PSNR_{ampl} for amplitude. These results are shown for five values of σ varying from the nearly noiseless data ($\sigma = .1$) to very difficult reconstructions from the high level noise observations with $\sigma = 0.9$. The following notation is used for the algorithms in this table. BM_1 and BM_2 stand for CD-BM3D and iterative CD-BM3D, respectively. Sp denotes the SpInPhase algorithm, and WFT stands for the WFT algorithm. The column *Surf* indicates phase test-image. The best results are marked in bold which

FIG. 4.2. *Absolute phase surfaces: (from left to right) truncated Gaussian, shear planes, continuous sinusoidal, discontinuous sinusoidal, mountains. In each small image we show the true surface (left) and the iterative CD-BM3D reconstruction (right).*

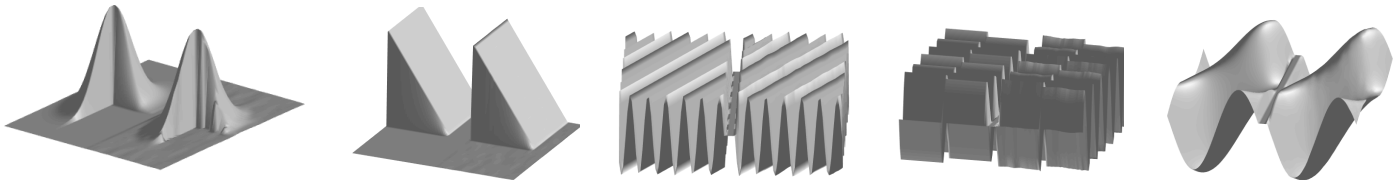

are for the interferometric phase reconstruction (column PSNR_{φ}) are always in BM_2 columns.

The comparison of CD-BM3D versus iterative CD-BM3D shows to what extend the iterations improve CD-BM3D. The interferometric phase reconstruction is of special interest (column PSNR_{φ}). For the truncated Gaussian phase the advantage of BM_2 is clear for $\sigma < 0.9$ with a PSNR improvement about 0.6 dB. For $\sigma = 0.9$ the accuracy of BM_1 and BM_2 are identical. Comparison of these algorithm with respect to both Sp and WFT is definitely in favor of BM_1 and BM_2.

For other phase test-images the advantage of BM_2 with respect to BM_1 is even more definite. The strongest improvement $1.3 - 2.4$ dB is demonstrated for the sinusoidal continuous phase. For the share planes the improvement is varying from 1 dB to 2.7 dB. For the sinusoidal discontinues and mountains the improvement in PSNR_{φ} is from 0.4 dB to 1.1 dB. The comparison with respect to Sp and WFT is always in favor of the CD-BM3D algorithms.

Comparison of $\mathrm{RMSE}_{\varphi_{abs}}$ and PSNR_{ampl} gives similar but not identical conclusions again mainly in favor of both BM_1 and BM_2, while sometime best results are demonstrated by Sp. Note that the parameters of Sp and WFT for this set of test-images are optimized in [21].

The test-images in this section are characterized by piece-wise smooth absolute phase surfaces of a large variation range (from 10 to 90 radians) leading to quite complex fringe patterns for wrapped phases. A direct application to these noisy fringes the standard strong denoisers, for instance the BM3D filter, is not successful (e.g. [29], [31]). The state-of-the-art performance of the algorithms compared in this section are mainly due to their functioning in the complex domain.

TABLE 4.1
ACCURACY OF PHASE AND AMPLITUDE RECONSTRUCTION: CD-BM3D (BM_1), CD-BM3D ITERATIVE (BM_2), SpInPhase (Sp) AND WFT.

Surf.		PSNR_{φ}				$\mathrm{RMSE}_{\varphi_{abs}}$				PSNR_{ampl}			
	σ	BM_1	BM_2	Sp	WFT	BM_1	BM_2	Sp	WFT	BM_1	BM_2	Sp	WFT
Trunc. Gauss.	.1	50.42	**50.94**	48.06	47.56	**.**019	**.018**	.025	.026	35.61	**36.15**	31.84	18.46
	.3	43.86	**44.44**	42.05	40.25	.040	**.037**	.050	.061	28.28	**28.98**	26.05	17.06
	.5	39.66	**40.00**	38.76	36.69	.065	**.060**	.072	.091	23.91	**24.96**	23.24	15.71
	.7	36.57	**37.46**	36.08	34.23	.678	**.083**	.364	.63	20.93	**22.32**	20.44	14.70
	.9	33.86	**33.89**	33.47	32.24	1.11	1.11	**.315**	1.49	18.28	**20.58**	15.99	13.83
Shear plane	.1	56.90	**58.17**	58.01	48.25	.009	**.007**	.008	.024	40.58	41.88	**43.06**	18.45
	.3	48.73	**49.44**	49.02	40.93	.028	.023	**.021**	.056	31.04	32.60	**32.86**	17.08
	.5	44.37	**46.66**	43.65	37.36	.038	**.029**	.043	.085	27.80	**30.22**	26.77	15.76
	.7	41.46	**43.97**	40.15	35.06	.053	**.040**	.061	.111	24.73	**27.44**	21.71	14.77
	.9	39.05	**41.78**	33.65	33.17	.070	**.051**	.131	.138	22.19	**25.21**	14.28	13.92
Sinus. cont.	.1	56.65	**57.98**	56.26	43.87	.009	**.008**	.009	.043	40.58	**41.71**	37.65	17.88
	.3	47.09	**48.54**	47.92	35.84	.028	**.023**	.025	.102	28.14	29.26	**32.91**	15.30
	.5	42.25	**44.05**	43.22	32.09	.048	**.039**	.043	.161	23.81	24.99	**27.32**	13.36
	.7	38.52	**40.85**	40.68	29.41	.074	**.057**	.058	.226	20.46	22.27	**24.78**	11.63
	.9	35.48	**37.86**	36.29	27.29	.105	**.080**	.096	.315	17.41	20.04	**22.08**	10.24
Sinus. disc.	.1	55.53	**56.40**	48.08	43.87	.010	**.010**	.024	.04	39.58	**40.59**	30.71	18.06
	.3	45.85	**46.34**	44.16	35.84	.032	**.030**	.037	.10	29.86	**30.41**	27.59	15.78
	.5	41.33	**42.00**	39.54	32.09	.054	**.050**	.057	.16	25.31	**25.78**	24.63	14.01
	.7	38.00	**38.72**	36.08	29.41	.079	**.730**	.092	.21	22.34	**22.71**	21.17	12.50
	.9	35.2	**36.34**	33.93	27.29	.109	**.095**	.125	.29	19.95	**20.67**	19.07	11.14
Mount.	.1	46.03	**46.84**	46.20	46.81	.031	**.028**	.030	.028	30.69	**31.75**	31.02	18.45
	.3	40.99	**41.25**	40.32	39.54	.056	**.053**	.061	.066	25.39	**25.56**	25.07	16.98
	.5	36.73	**37.04**	36.84	35.97	.091	**.088**	**.088**	.100	21.42	**21.73**	21.71	15.63
	.7	33.86	**34.37**	33.20	33.51	.127	**.120**	.123	.132	18.75	**19.34**	18.99	14.56
	.9	31.54	**32.31**	32.25	31.63	.166	0.152	**.149**	.165	16.31	**17.43**	16.47	13.59

4.2.2. Natural images. Cameraman and Lena images (256×256) typical for image processing studies are used in these tests. For phase modeling these images are scaled to the interval $[0\ \pi/4]$ in order to avoid problems caused by phase wrapping and unwrapping. The goal of these tests is to evaluate how good are the developed algorithms for phase images of complex geometrical structure full of small details.

The results shown in Table 4.2 are in favor of iterative CD-BM3D (BM_2) for the phase reconstruction and in favor of SpInPhase for the amplitude reconstruction . Comparing CDBM3D versus iterative CDBM3D we may note that the improvement in the phase imaging due to the iterations is about 0.7 dB. However, for the amplitude reconstruction on many occasions CDBM3D preforms better than iterative CDBM3D with the advantage about 0.6 dB.

The phase imaging achieved by iterative CDBM3D is illustrated for 128×128 fragments of the test-images in Figs.4.3-4.4. For comparison we show also the phase images of the noisy complex-valued observations. The input data of the algorithm are

TABLE 4.2
ACCURACY OF PHASE AND AMPLITUDE RECONSTRUCTION: CD-BM3D (BM_1), CD-BM3D ITERATIVE (BM_2), SpInPhase (Sp) AND WFT.

Image		PSNR_{φ}				PSNR_{ampl}			
	σ	BM_1	BM_2	Sp	WFT	BM_1	BM_2	Sp	WFT
Lena	.1	45.66	**46.17**	41.43	45.42	35.61	34.39	**38.24**	22.31
	.3	39.64	**40.29**	38.48	39.16	29.89	29.13	**31.31**	20.61
	.5	36.89	**37.67**	36.73	36.30	26.42	26.61	**29.40**	19.01
	.7	35.02	**35.87**	34.44	34.42	23.86	24.66	**27.25**	17.73
	.9	33.71	**34.55**	34.14	32.93	21.76	23.07	**24.69**	16.60
Cameraman	.1	44.06	**44.53**	41.00	43.79	35.50	34.60	**36.22**	22.21
	.3	39.02	**39.56**	37.89	38.00	29.45	29.20	**29.75**	20.50
	.5	36.30	**37.04**	35.97	35.35	26.07	26.38	**28.81**	18.86
	.7	34.41	**35.25**	34.17	33.59	23.60	**24.51**	26.49	17.61
	.9	33.11	**33.92**	33.28	32.21	21.60	**23.04**	23.00	16.51

quite noisy and the reconstructed images are of quite a good quality. The improvement due to this processing in $PSNR$ is about 10 dB.

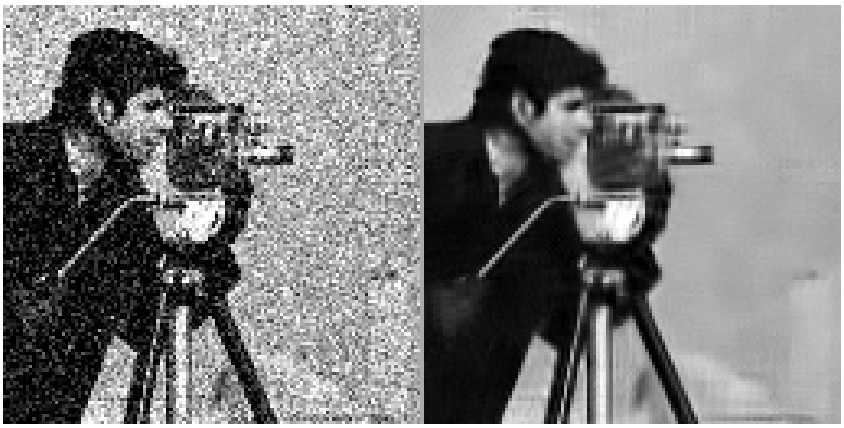

FIG. 4.3. *Cameraman phase images: noisy phase observation (left) and iterative CDBM3D phase reconstruction (right),* $\sigma = 0.3$. *PSNR for the reconstruction is* 39.56 *dB and for the noisy phase is* 29.22 *dB.*

Further, we consider different type experiments. Let us assume that both phase and amplitude are spatially varying and varying in different ways. In these tests cameraman is used as a phase and Lena as an amplitude. The phase is scaled to the interval $[0\ \pi/4]$ and the amplitude to the interval [0.1 1.1]. The latter is done in order to avoid zero or close to zero values for amplitude.

Figs.4.5 and 4.6 show the results obtained for the noiseless and small level noise ($\sigma = 0.1$) scenarios. The columns in these images from left-to-right correspond to the BM_2, Sp and WFT algorithms. In the noiseless case the phase reconstruction is quite successful for all algorithms. Nevertheless the best result are by BM_2: Sp produces an oversmoothed imaging and details given by WFT are not so clean and sharp as

FIG. 4.4. *Lena phase images: noisy phase observation (left) and iterative CDBM3D phase reconstruction (right),* $\sigma = 0.3$. *PSNR for the reconstruction is* 40.29 *dB and for the noisy phase is* 29.27 *dB.*

those in BM_2 imaging.

The amplitude reconstruction (Lena) is not so good. In particular, we may note traces of the phase cameraman profile on Lena's hat. In the most obvious form it is seen in the Sp image.

Noisy data in this scenario with Lena for phase and cameraman for amplitude result in a serious degradation of both phase and amplitude reconstructions (Fig.4.6). The Sp phase image is again oversmoothed but visually it is even better than the corresponding Sp phase image for the noiseless case. Both phase reconstructions for BM_2 and WFT are damaged by strong artifacts, while BM_2 looks better. For the amplitude reconstruction again visual quality is better for BM_2 as compared with Sp and WFT.

FIG. 4.5. *Reconstruction of varying phase (cameraman) and amplitude (Lena): from left-to-right: BM_2, Sp, WFT algorithms, noiseless observations, $\sigma = 0$.*

In the following more sophisticated tests we assume that the phase is a sum of two terms: cameraman as it is in the previous test and a quadratic phase. This quadratic phase component is typical for coherent optics experiments. It imitates effects of a spherical wave impinging on the phase object. In this case the absolute phase in the model (2.1) is of the form $\varphi_{abs} = \varphi_{quad} + \varphi_o$, where φ_o stands for the object phase (cameraman) and φ_{quad} is the quadratic phase term. The wrapped phase of the observed z is shown in Fig.4.7, where the circular fringes appear due to φ_{quad} of the range upto 20 radians. The features of the cameraman can be recognized as a background (or foreground) of these fringes. The noise effects are clearly seen in these phase images. Iterative CD-BM3D was used for the phase reconstruction. After unwrapping this reconstruction gives an absolute estimate $\hat{\varphi}_{abs}$. The range of the object phase equal to $\pi/4$ is much smaller than 20 radian variations of φ_{quad}. In order to make visible the object phase reconstruction we show in Fig.4.8 a difference $\hat{\varphi}_{abs} - \varphi_{quad}$ as an estimate of φ_o. The quality achieved for the object phase reconstruction is quite good naturally degrading as soon as the noise standard deviation becomes larger.

4.2.3. Computational complexity. The theoretical complexity analysis produced in [20] for real domain BM3D with incorporated HOSVD for basis design is completely applicable to CDBM3D. In particular, it is shown that provided fixed parameters of the algorithm the computational time is proportional to the image size. One can see also in [20] the asymptotic for influence of the patch size and group length on the computational time.

We are focussed on a different task: experimental comparative analysis of the algorithms tested in this section. In all experiments we use the same complex-valued image rescaled to different sizes. Lena is selected as a test-image for the phase and

FIG. 4.6. *Reconstruction of varying phase (cameraman) and amplitude (Lena): from left-to-right: BM_2, Sp, WFT algorithms, noisy observations, $\sigma = 0.1$.*

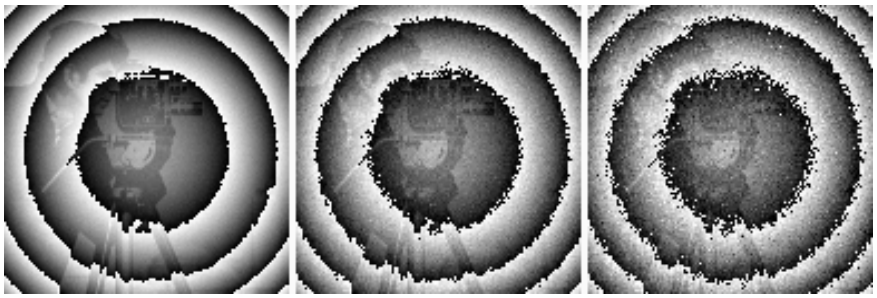

FIG. 4.7. *Noisy observation phase. From left to right $\sigma = 0.1$, $\sigma = 0.3$, $\sigma = 0.5$.*

the amplitude is invariant equal to 1.

In Table 4.3 we show the mean values of the computational time obtained for different size images. The averaging is done over the computational times calculated for $\sigma = [0.1, 0.3, 0.5, 0.7, 0.9]$. For the smallest size image, 100×100, BM_1 is the fastest algorithm: twice faster than WFT and about 20 times faster than Sp. For larger size images the computational time of BM_1 and WFT is nearly equal and BM_2 is the slowest algorithm.

Note that the computations time for BM_1 is about proportional to the image size, what is in agreement with the asymptotic result in [20].

Further analysis was done in order to know how the computational time of BM_1 is distributed between $BM3D$ and $HOSVD$ operations. This time sharing is more or less the same for all image sizes. Roughly speaking, it is about 70% for $BM3D$ and about 25% for $HOSVD$.

FIG. 4.8. *Reconstruction of absolute phase minus quadratic background phase, iterative CD-BM3D algorithm. From left to right* $\sigma = 0.1$, $\sigma = 0.3$, $\sigma = 0.5$.

TABLE 4.3
COMPUTATION TIME IN SEC. ALGORITHMS: CD-BM3D (BM_1*), CD-BM3D ITERATIVE (*BM_2*, 5 ITERATIONS), SpInPhase (Sp) AND WFT*

Im. Size\ Alg.	BM_1	BM_2	Sp	WFT
100×100	4.2	18.3	81.8	10.6
256×256	27.6	136.2	100.3	23.0
512×512	120.2	603.5	216.4	117.4
1024×1024	465	2330	1503	419

4.3. Sparsity of CD-BM3D modeling. The complex domain sparsity implemented in CD-BM3D algorithms is discussed in this section.

Remind that for each reference pixel we build a $3D$ array (group) and apply HOSVD in order to get the corresponding $3D$ core array (complex domain spectrum). The maximal number of items in the $3D$ group core-tensor is $8 \times 8 \times 32 = 2048$, where 32 is the maximal length of the group. For each of these groups HOSVD calculates three orthonormal transform matrices (dictionaries) of sizes 8×8, 8×8 and 32×32.

In Fig.4.9 we show an example of these transform matrices as they are calculated for the 128×128 image with cameraman for phase and Lena for amplitude in the noiseless scenario. Small rectangles in Fig.4.9 are 8×8 transforms applied to the vertical columns of $3D$ groups. We use *red* for phases and *blue* for amplitudes of these complex-valued transforms. Fig.4.9 qualitative illustrates a variety of the transforms generated in CD-BM3D. Each of these 8×8 transforms is built for non-local areas of patches similar to the corresponding reference patch.

The number of these transforms, 1681 in this image, is equal to the total number of the reference patches. Remind that not all pixels are used to define reference patches. In the considered test it is every third pixels in each row and each column. The ratio of the total number of the reference patches to the image size is $128 \cdot 128/1681 \simeq 10$.

Thus, for the 128×128 image we calculate 1681 HOSVD transforms. For each 3D group we have the core tensor of the maximal size $8 \times 8 \times 32 = 2048$ with the total number of the spectral elements (elements of the core tensors) for the image equal to $2048 \cdot 1681 = 3442688$.

Compared with the image size $128 \times 128 = 16384$ the HOSVD spectral representation enables a huge redundancy in the transform domain, $3442688/16384 \simeq 200$. However, after thresholding the total number of the non-zero (active) spectral elements is about 11090. Thus the ratio $3442688/11090 \simeq 300$ is the sparsity achieved

in the spectral domain.

These calculations clarify explicitly what kind of sparsity is appeared in the developed algorithms. For image analysis the huge overcomplete number of the spectral elements are produced and only tiny part of them is used for imaging as they are selected by the thresholding procedures.

In this test the ratio of the number of active spectral elements to the image size is $16384/11090 \simeq 1.5$. The main goal of this sparsity development is the image quality but not the image compression.

Fig.4.10 is the distribution (histogram) of the active spectral elements: a number of groups (vertical axis) generated by CD-BM3D versus a number of the active spectral elements (horizontal axis). This distribution has a maximum at 10 showing that 140 groups have 10 active spectral components. Numbers of the groups having smaller or larger values of the active spectral items can be very small.

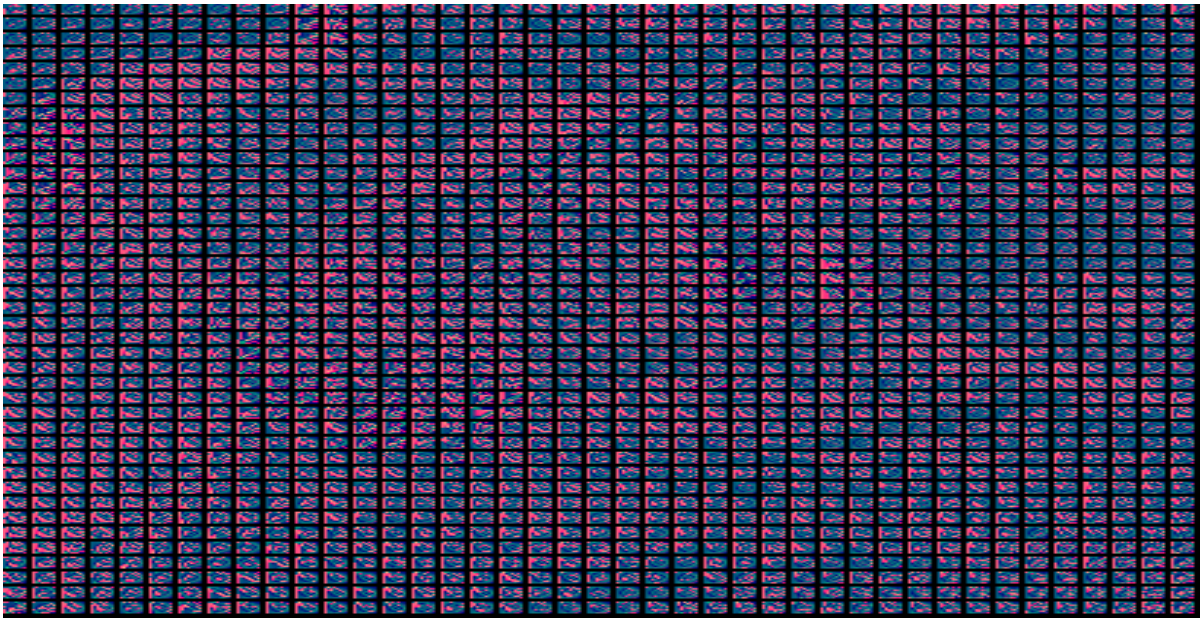

FIG. 4.9. *Complex-valued* 8×8 *transform matrices for noiseless data with varying phase (cameraman) and varying amplitude (Lena). Visualization is produced by red and blue colours, respectively, for angles and amplitudes of elements of the complex-valued transforms.*

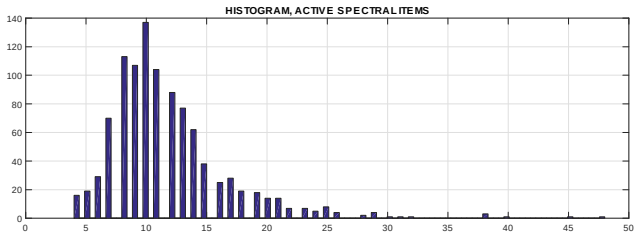

FIG. 4.10. *Histogram of the number of active (nonzero) elements of the core (spectral) tensor,* $\sigma = 0.5$*, phase image mountains and amplitude is equal to* 1.

5. Concluding remarks. This paper introduces CD–BM3D and iterative CD–BM3D, as effective algorithms for interferometric phase image estimation, that is, the estimation of phase modulo-2π images from sinusoidal 2π-periodic and noisy observations. The problem is formulated as estimation of the true complex-valued image via spectral sparse representation for 3D grouped data. Complex domain spectral representations of these BM3D groups are obtained by HOSVD factorization of the 3D data. The filtering of the HOSVD spectrum is produced using component wise hard-thresholding. In a series of experiments with simulated data, CD–BM3D and iterative CD–BM3D algorithms mainly produced better estimates than the SpInPhase and WFT algorithms which are the state-of-the-art in the field.

Through the extensive testing we found that CD–BM3D is an nonexpansive operator. This observation is a base for the convergence proof for iterative CD–BM3D.

The following versions of the CD–BM3D algorithms have been tested in process of the algorithm's development: soft-thresholding in CD-BM3D and 2D SVD transform instead of 3D HOSVD. It is found that the hard-thresholding and 3D HOSVD enable better performance.

The complex domain BM3D-style Wiener filtering as a postprocessing for CD-BM3D was developed and tested. It was found that this algorithm demonstrates an improvement in performance with respect to the CD-BM3D with PSNR results between those for CD-BM3D and iterative CD-BM3D.

6. Acknowledgement. The authors are thankful to Alessandro Foi for fruitful discussions.

REFERENCES

[1] R. K. Tyson. *Principles of Adaptive Optics*. 4rd ed., CRC Press, 2014.
[2] L. Wang and H. Wu. *Biomedical Optics: Principles and Imaging*. John Wiley & Sons, Inc., 2007.
[3] B. Kress and P. Meyrueis. *Applied Digital Optics: From Micro-Optics to Nanooptics*. John Wiley & Sons, Inc., 2009.
[4] A. Patil and P. Rastogi, "Moving ahead with phase," Optics and Lasers in Engineering, vol. 45, no. 2, pp. 253-257, 2007.
[5] Th. Kreis, *Handbook of Holographic Interferometry*. Wiley-VCH, Berlin, 2005.
[6] J. Glückstad, and D. Palima. *Generalized phase contrast: applications in optics and photonics*. Springer Series in Optical Sciences, vol. 146, 2009.
[7] M. Elad. *Sparse and Redundant Representations: from Theory to Applications in Signal and Image Processing*. Springer, 2010.
[8] S. Gazit, A. Szameit, Y. C. Eldar, M. Segev, "Super-resolution and reconstruction of sparse sub-wavelength images, " *Optics Express* **17**, pp. 23920-23946, 2009.
[9] Y. Shechtman, Y. C. Eldar, O. Cohen, H. N. Chapman, J. Miao, and M. Segev, "Phase retrieval

with application to optical imaging: a contemporary overview," *IEEE Signal Processing Magazine*, pp. 87-109, 2015.

[10] Z. Xu and E. Y. Lam , "Image reconstruction using spectroscopic and hyperspectral information for compressive terahertz imaging", *J. Opt. Soc. Am. A*, **27**, Issue 7, pp. 1638-1646, 2010.

[11] V. Katkovnik and J. Astola, " High-accuracy wavefield reconstruction: decoupled inverse imaging with sparse modeling of phase and amplitude, " *J. Opt. Soc. Am. A*, **29**, pp. 44 – 54, 2012.

[12] V. Katkovnik and J. Astola, "Sparse ptychographical coherent diffractive imaging from noisy measurements," *J. Opt. Soc. Am. A*, vol. 30, 367-379, 2013.

[13] V. Katkovnik and J. Astola, "Compressive sensing computational ghost imaging," *J. Opt. Soc. Am. A*, vol. 29, no. 8, pp. 1556-1567, 2012.

[14] A. Bourquard, N. Pavillon, E. Bostan, C. Depeursinge, and M. Unser, "A practical inverse-problem approach to digital holographic reconstruction," Optics Express, **21**, no. 3, pp. 3417-3433, 2013.

[15] K. Dabov, A. Foi, V. Katkovnik, and K. Egiazarian, "Image denoising by sparse 3D transform-domain collaborative filtering", *IEEE Trans. Image Process.*, **16**, no. 8, pp. 2080-2095, 2007.

[16] L. De Lathauwer, B. De Moor, J. Vandewalle, "A multilinear singular value decomposition," *SIAM J. Matrix Anal. Appl.* **21**, pp. 1253–1278, 2000.

[17] L.R. Tucker, "Some mathematical notes on three-mode factor analysis," *Psychometrika* **31**, pp. 279–311, 1966.

[18] P.M. Kroonenberg, J. De Leeuw, "Principal component analysis of three-mode data by means of alternating least squares algorithms," *Psychometrika* 45 (1) pp. 69–97, 1980.

[19] Foi, A., V. Katkovnik, and K. Egiazarian, "Pointwise shape-adaptive DCT for high-quality denoising and deblocking of grayscale and color images", *IEEE Trans. Image Process.*, **16**, no. 5, pp. 1395-1411, 2007.

[20] A. Rajwade, A. Rangarajan and A. Banerjee, "Image denoising using the higher order singular value decomposition," *IEEE Trans. on Pattern Analysis and Machine Intelligence*, **35**, no. 4, pp. 849-862, 2013.

[21] H. Hongxing, J. M. Bioucas-Dias, and V. Katkovnik, "Interferometric phase image estimation via sparse coding in the complex domain," *IEEE Trans. on Geoscience and Remote Sensing*, vol. 53, no. 5, pp. 2587 - 2602, 2015.

[22] V. Katkovnik, K. Egiazarian, J. Bioucas-Dias,'Phase imaging via sparse coding in the complex domain based on high-order SVD and nonlocal BM3D techniques,' *Proceedings of IEEE International Conference on Image Processing (ICIP 2014)*, pp. 4587-4591, 2014.

[23] D. Donoho and I. Johnstone, "Ideal spatial adaptation by wavelet shrinkage," *Biometrika*, vol. 81, pp. 425-455, 1993.

[24] D. C. Ghiglia and M. D. Pritt. *Two-Dimensional Phase Unwrapping: Theory, Algorithms, and Software*. Wiley, 1998.

[25] A. Danielyan, V. Katkovnik, and K. Egiazarian, " BM3D frames and variational image deblurring, " *IEEE Trans. Image Process.*, **21**, pp. 1715 – 1728, 2012.

[26] M. Elad, P. Milanfar, and R. Rubinstein, Analysis versus synthesis in signal priors, *Inverse Problems*, **23**, no. 3, pp. 947-968, 2007.

[27] F. Facchinei and C. Kanzow, "Generalized Nash equilibrium problems," *4OR, Quart. J. Oper. Res.*, vol. 5, no. 3, pp. 173–210, 2007.

[28] Q. Kemao, "Two-dimensional windowed Fourier transform for fringe pattern analysis: Principles, applications and implementations," *Optics and Lasers in Engineering,* vol. 45, no. 2, pp. 304 – 317, 2007.

[29] Q. Kemao, Q., *Windowed fringe pattern analysis*. SPIE Press, (2013).

[30] J. M. Bioucas-Dias and G. Valadão, "Phase unwrapping via graph cuts," *IEEE Trans. Image Process*, **16**, no. 3, pp. 698–709, 2007.

[31] M. Zhao, Q. Kemao, "A comparison study of denoising techniques in fringe pattern analysis," *Internal. Conf. on Experimental Mechanics*, 2014, Proc. of SPIE vol. 9302, 930208-1-930208-6, 2014.